

# Ray-tracer for modeling interactions of light with space objects

Olli Wilkman

*Finnish Geospatial Research Institute FGI*

## ABSTRACT

A simulation tool has been developed for modeling the interaction between light and objects in space. It is based on a ray-tracing framework, computing the flow of radiative energy in a system consisting of an object and various light sources. The software is modular on many levels. The core ray-tracing simulation can be used with different output modules to compute e.g. a visual image, integrated (non-resolved) photometry, radiation pressure forces and torques, or the pulse shapes of reflected laser ranging pulses. Inside the simulation, different shape models and surface scattering models can be plugged in. The first main application of the software is the simulation of an satellite laser ranging (SLR) pulse reflected by a space debris object. Laser ranging can be performed even on objects without retro-reflectors, as long as they are large and near enough. However, the reflected pulse is not as well-defined, and depends on the shape and material properties of the object, affecting the observed photon statistics. We compute the reflected pulse shapes from various objects and generated simulated SLR observation data. This data can be used to better estimate the observability of various debris objects with a given SLR system. It will also help in developing methods for extracting information, such as the rotational state, of the target body from SLR observation. Another application is simulating non-resolved photometry and spectrometry of space debris when observed with small telescopes.

## 1.

### INTRODUCTION

We present one application of a general-purpose tool designed for simulating the interactions between space objects and light. We have performed simulations of laser pulse reflections from various objects in idealized conditions and created simulated SLR data in these situations.

Satellite laser ranging (SLR) is a technique for measuring accurate distances between a ground station and orbiting satellites. It's most important applications are in geodesy, where the precise orbit determination (POD) of special geodetic satellites is used for measuring the Earth's gravity field and maintaining reference frames [1]. SLR can also be used for POD of regular satellites, and is used where high precision positions and orbits are required, such as positioning systems and certain Earth observation satellites [2].

In satellite laser ranging, laser pulses are transmitted from a ground station towards a satellite, where they are reflected back, and the returning photons are detected by a telescope system. The flight time of the laser pulses are measured, and give the range between the station and the target, after various corrections for timing errors, atmospheric effects etc. are performed [1].

Traditionally, the effective use of SLR requires the target satellite to be equipped with retro-reflectors ("co-operative targets"), which efficiently reflect the incoming laser pulse back towards the SLR station. With such targets, ranging accuracies can be in the order of millimetres, which is required for geodetic work. In recent years, experiments have been ongoing in laser ranging to targets without retro-reflectors ("non-cooperative targets"), particularly space debris [3]. Laser ranging allows better orbit determination to debris targets, which is particularly important in re-entry situations, where the object's orbit can change rapidly and unpredictably due to aerodynamic forces.

Laser ranging to non-cooperative targets is significantly more difficult. Firstly, without retro-reflectors, the reflected pulse is several orders of magnitude less bright. Secondly, with retro-reflectors, the reflection comes from a relatively well-defined point on the target's surface. Without them, the reflections come from all over the target body, reducing ranging accuracy.

An SLR system optimized for geodetic work is not optimal for space debris ranging due to a trade-off between laser

pulse width and power: geodetic observations require high accuracy, which means the shortest laser pulse widths possible. Because the retro-reflectors effectively reflect the pulse back, the laser power does not need to be very high. On the other hand, when observing space debris, the ill-defined reflection negates the advantage from narrow pulse width, while a more powerful laser is required due to the weak reflection.

Laser ranging can be used to determine the rotation states of space objects. A modern SLR system can transmit thousands of pulses per second, providing a high temporal resolution in the ranging. When a co-operative target rotates, the rotation of the retro-reflector around the centre of mass modulates the observed range, and can be observed by subtracting the orbital motion. The evolution of the rotational states of various decommissioned satellites, such as TOPEX/Poseidon have been studied through SLR [4].

With non-cooperative targets, the study of the rotational state through ranging is significantly more difficult due to the reasons described above. To our best knowledge, no results of this kind have yet been published. However, as new and upgraded SLR systems proliferate and space surveillance activities expand, we such experiments to begin.

## 2. MODULAR RAYTRACER

To simulate SLR pulses, we use a generic ray-tracer algorithm. The structure of the software is based on the textbook example from [5] and written in the Julia language [6]. It has been greatly simplified where possible, and additional modularity has been added where necessary. The user determines the shape model and its surface reflection properties, the illumination, and the detector. These are then passed to the ray-tracer core, which computes the transfer of energy between the light sources and the detector. The output is then retrieved from the detector.

The detector is an abstraction which depends on the desired output product. The simplest detector is a one-pixel spectrometer, defined as a camera with a given aperture and field of view, which integrates all the light entering it into one spectrum sum. A more complicated detector could model a hyper-spectral camera, but this has not been implemented yet. For visualization, we can use an RGB camera, which outputs a JPEG image approximating human vision.

More sophisticated detectors can also be implemented. The “radiation pressure integrator” collects information on the momentum transferred by the rays onto the target object, and outputs the net force and torque produced by the illumination. The detector used in this work is the “delay camera”. For each ray, the distance travelled inside the simulation volume is measured, and the detector collects a histogram of backscattered spectral radiance as a function of photon travel time.

The shape model can be composed of elementary geometric shapes: spheres, cylinders, disks, etc., as well as triangle meshes. Each component can have a separate reflection model.

The currently used reflection models are Lambertian, mostly used for testing purposes, and Ashikhmin-Shirley [7], used to model man-made space objects. Currently, only simple surface-scattering is modeled, and wavelength-dependent reflection or polarization properties are not implemented. Multiple scattering is supported but not used in the pulse delay computations presented here.

The Ashikhmin-Shirley BRDF used in this study is based on the form given in [8], with the assumption of an isotropic surface, and has the form

$$R(\hat{\omega}_i, \hat{\omega}_o) = dR_d + sR_s, \quad (1)$$

where

$$R_d = \frac{28\rho}{23\pi} (1 - sF_0) \left( 1 - \left( 1 - \frac{\hat{n} \cdot \hat{\omega}_i}{2} \right)^5 \right) \left( 1 - \left( 1 - \frac{\hat{n} \cdot \hat{\omega}_o}{2} \right)^5 \right) \quad (2)$$

$$R_s = \frac{n+1}{8\pi} \frac{F}{(\hat{\omega}_o \cdot \hat{h}) \max[\hat{n} \cdot \hat{\omega}_i, \hat{n} \cdot \hat{\omega}_o]} (\cos \alpha)^n \quad (3)$$

and the Fresnel factor

$$F = F_0 + \left( \frac{1}{s} - F_0 \right) \left( 1 - \hat{\omega}_o \cdot \hat{h} \right)^5. \quad (4)$$

The vectors  $\hat{\omega}_i$  and  $\hat{\omega}_o$  are the incident and emergent directions,  $\alpha$  is the phase angle (the angle between these two vectors),  $\hat{n}$  is the surface normal, and  $\hat{h}$  is the scattering half-angle vector,  $\hat{h} = (\hat{\omega}_i + \hat{\omega}_o)/2$ . The parameter  $F_0$  is the surface reflectance at normal incidence while  $\rho$  is the diffuse reflectance. Following [8] we set  $F_0 = \rho$ . The parameter  $d$  is the fraction of diffuse reflectance, with  $d = 1$  purely diffuse and  $d = 0$  purely specular, and  $s = 1 - d$ . The parameter  $n$  controls the width of the specular peak, with larger  $n$  meaning a narrower peak.

The ray-tracer simulation and the “delay camera” is used to compute the time-resolved reflection of a laser pulse from a shape model. The incident light is assumed to be infinitely distant (i.e. its rays are parallel). The incident radiance is set to unity here, and scaled to model the transmitting power and distance of a particular SLR system at the next step. The output is a histogram of radiance at 532 nm as a function of delay.

This time-resolved reflection must then be scaled properly to simulate actual observations. The value also needs to be convolved with the transmitted pulse to get the true reflected pulse. For simplicity, we assume here that the transmitted pulse is narrow compared to the time resolution we study, and define it as a delta distribution. The convolution therefore simplifies to a multiplication by the total transmitted pulse energy. We also need to factor in the distance between station and target, the aperture of the receiver, and the number of photons per Joule at the laser wavelength. Finally we have an intensity function in units of photons/nanosecond (Fig. 1).

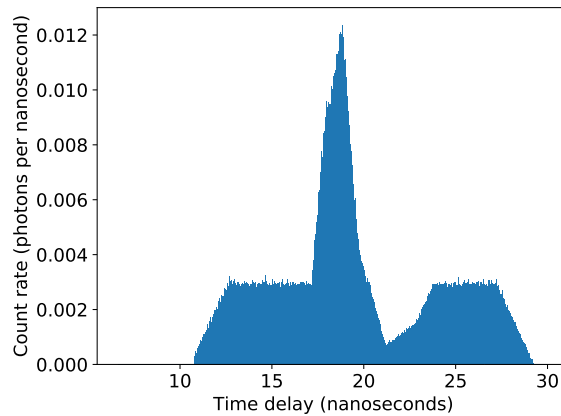


Fig. 1: An example of the received pulse shape from a box-wing shape model (see below). In this orientation, the reflections from the different parts can be discerned. The two wings are much fainter than a facet of the box in the middle, which has a stronger specular component.

### 3.

### LASER RANGING PULSE STATISTICS

Given the reflected laser pulse shape, a sequence of laser ranging observations can be simulated. In an SLR system, the transmitted laser pulse triggers an accurate interval timer. Shortly before the reflected pulse is expected to return (based on a priori knowledge of the target's orbit), a single-photon detector is armed. When a photon hits the detector, the interval timer stops, and the elapsed time interval is recorded. Many of the photons detected by the system will be noise, but when enough pulses have been fired, the true distance can be distinguished from the observed distribution of time intervals. The probability of a noise photon is greater the longer the detector is armed. Because the detector is only armed for a finite time  $\Delta t$ , it is possible that no photon arrives during that interval. This means that a single pulse observation produces either the arrival time of a photon, or the result "no photon".

The single-photon observations are statistically modeled as a non-homogeneous Poisson process. If the intensity of the photon source is  $\lambda(t)$  (photons/nanosecond), then the probability distribution function (PDF) of the wait time (in nanoseconds) until the first photon is

$$p(t|\lambda) = \lambda(t) \exp\left(-\int_0^t \lambda(t') dt'\right). \quad (5)$$

The intensity function is taken to be a sum of the signal from the target and a constant noise level,

$$\lambda(t) = \lambda_s(t) + \lambda_n. \quad (6)$$

The simulated observations are generated by sampling the probability distribution: A random number  $u$  is generated from the uniform distribution  $U(0, 1)$ . This is then compared to the cumulative distribution function (CDF), of the distribution,

$$F(t|\lambda) = \int_0^t p(t'|\lambda) dt'. \quad (7)$$

The point  $t$  where  $F(t) = u$  is the desired sample. If  $t \leq \Delta t$ , we return the value  $t$ , and in the other case we return "no photon". With a realistic intensity function, the integrals in the above equations become intractable to analytical methods, and must be computed numerically. In our work, the intensity function is numerically derived and discretized in time, so a numerical approach is required in any case.

### 4.

### RESULTS

We compute reflected pulse shapes from a variety of simple shape models. Presented here are three examples: a hexagonal prism, an elongated cylinder, and a simple box-wing satellite model.

We assume the distance between the station and the target is 1000 km. The size of the target varies between shape models, but is in the order of metres, with cross sections in the order of 1–10 square metres. The dimensions of each shape will be given below. The receiving telescope system has an effective area of a 0.5 m circle. The transmission pulse rate is set at 2000 pulses/second and the pulse energy is 80 mJ. A noise level of 0.001 photons/nanosecond is chosen.

The parameters of the Ashikhmin-Shirley scattering model are given a total of 12 different combinations of values. These values were chosen as they were used also in [8] and cover the extremes of the parameter space well.

$$\rho = \begin{cases} 0.1 & \text{Low reflectivity} \\ 0.5 & \text{Medium reflectivity} \\ 0.9 & \text{High reflectivity} \end{cases} \quad (8)$$

$$d = \begin{cases} 0.2 & \text{Specular} \\ 0.8 & \text{Diffuse} \end{cases} \quad (9)$$

$$n = \begin{cases} 50 & \text{Dull specular speck} \\ 500 & \text{Sharp specular peak} \end{cases} \quad (10)$$

The descriptions of the parameter values above will be used in the text. The computations are done with each of the 12 different combinations, but only a representative sample will be shown here, as many of the parameter sets produce visually similar results.

Fig. 2 shows the hexagonal prism shape model, rendered by the “RGB camera” of the ray-tracer. The orientation and illumination of the object correspond to those seen by the SLR system, and the colour is a human-visual approximation of a grey object illuminated by a 532 nm laser. The object is one metre tall and has a diameter of two metres. It is oriented as shown in the figure and rotates around its symmetry axis. Fig. 3 shows the simulated SLR observations of the hexagonal prism for four of the 12 reflection parameter sets used. The period of rotation is 20 seconds. Six peaks can be discerned by eye in the distribution of pulse ranges, but the effect of the rotation is relatively minor, as a hexagonal prism is nearly symmetric around the rotation axis. The more specular cases are less bright, as more of the reflected energy is in the specular peak, which does not point in the backscattering direction in the orientations modeled here.

Fig. 4 shows the cylinder shape model in three orientations. The cylinder is three metres tall and has a radius of one metre. It is rotating around an axis through the middle, perpendicular to the symmetry axis. Fig. 5 shows the simulated data for the cylinder. The cylinder has a rotational period of 40 seconds and the figure shows half of a rotation. The orientation is changed steps of  $2^\circ$ , which is visible in the images as a slight stepping. Here, the effect of the orientation is clear. When the cylinder is sideways to the observer, the reflections are centered around the middle of its “ridge”. As the cylinder turns, the reflections spread out as the side turns away from view and the bottom turns into view. When the bottom is pointing towards the observer, all reflections are coming from the same distance, with such a strong specular reflection that practically all of the observed photons come from this same distance.

Fig. 6 shows the box-wing satellite model in various orientations. Fig. 7 shows the simulated data for this model. The features caused by the two wings and the central box are clearly visible. Compare the  $0^\circ$  orientation to the pulse shape shown in Fig.1. Again, the more specular surface models are less bright, because the specular peak always points away from the observer. Even though the box-wing model is simple, it already has complex structure which may be detectable with an SLR system.

## 5. DISCUSSION AND FUTURE WORK

We have simulated SLR observations for various different shape models. For the less symmetric situations (cylinder and box-wing), the orientation can be clearly visible in the distribution of pulse delays. In these situations, good enough data could allow for a period determination, though methods for this are still under development.

The results shown here are first computations with a new tool. More sophisticated computations will follow as the software is developed and more real data are available. The shape models used in this study were simple and the assumptions for the SLR system’s properties were reasonable guesses. Future steps in this work will involve simulating more complex shape models and realistic observation conditions. In particular, the noise levels and target brightness will be considerably worse with a more realistic model of a current SLR system. Observational data of non-cooperative objects is currently sparse, and comparisons to real data, using realistic model parameters and conditions would be invaluable.

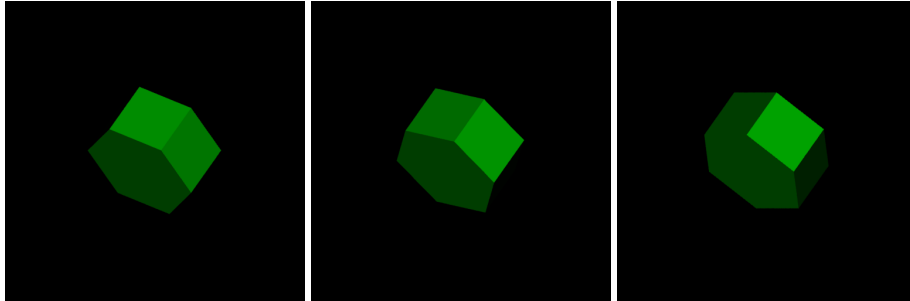


Fig. 2: The hexagonal prism in three orientations ( $0^\circ$ ,  $15^\circ$  and  $30^\circ$ ).

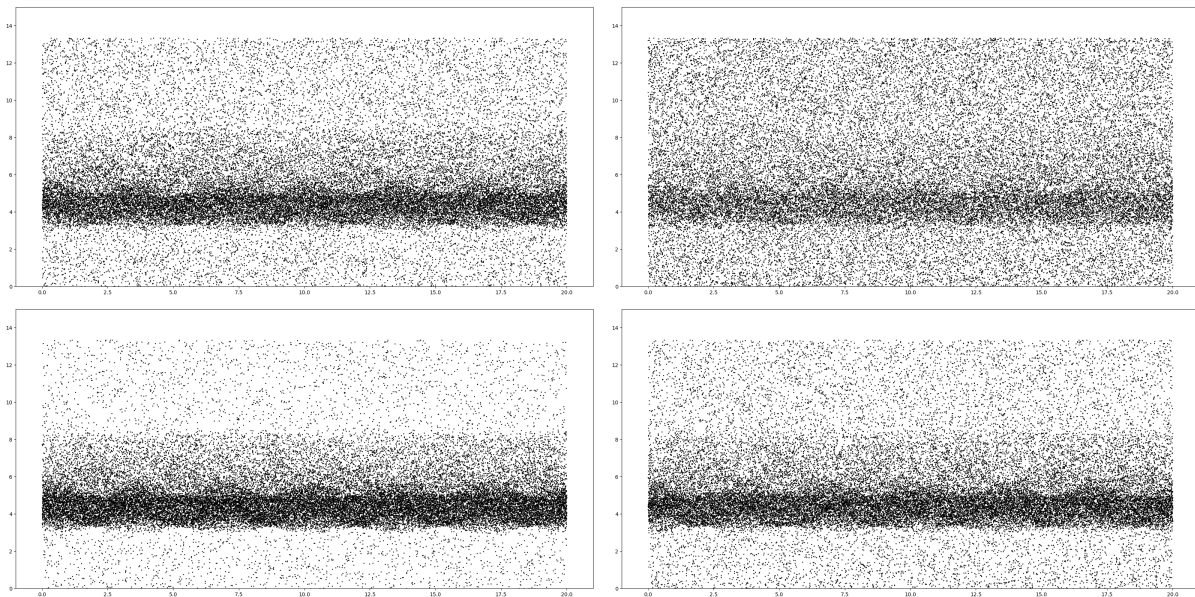


Fig. 3: Simulated SLR data for the hexagonal prism. On the horizontal axis, observational time in seconds. On the vertical axis, the delay of each laser pulse in nanoseconds with an arbitrary zero. From top left, by row: low reflectivity, diffuse; low reflectivity, specular; medium reflectivity, diffuse; medium reflectivity, specular. All images with a dull specular reflection. The width of the specular peak does now affect the data significantly.

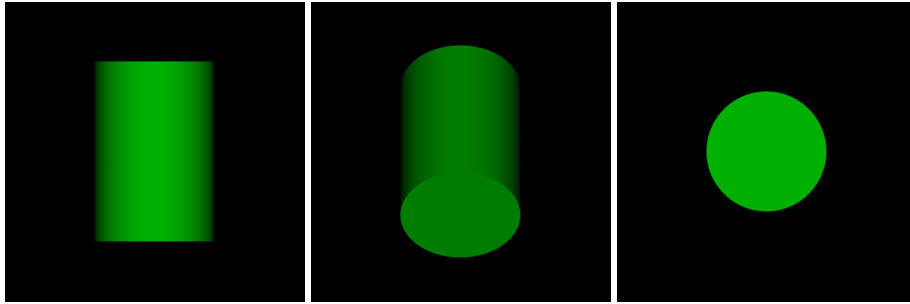


Fig. 4: The cylinder shape model in three different orientations ( $0^\circ$ ,  $45^\circ$  and  $90^\circ$ ). In these images, the cylinder is rendered with a Lambertian rather than Ashikhmin-Shirley reflection model for better contrast.

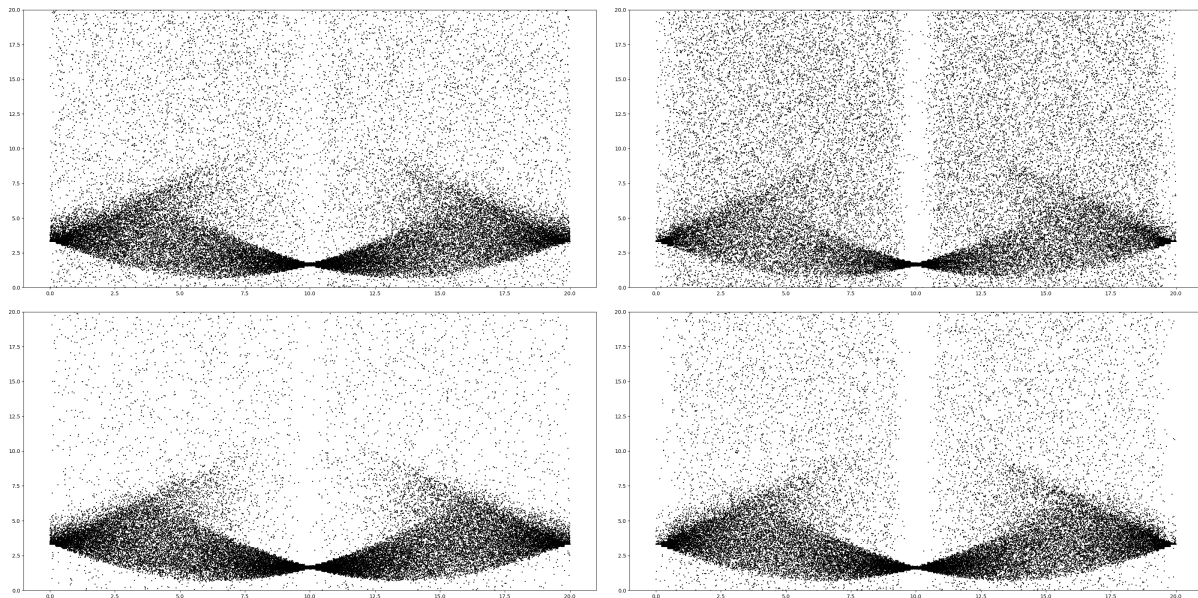


Fig. 5: As Fig. 3, for the cylinder shape model. Here, the rotation period is 40 seconds and half a rotation is shown.

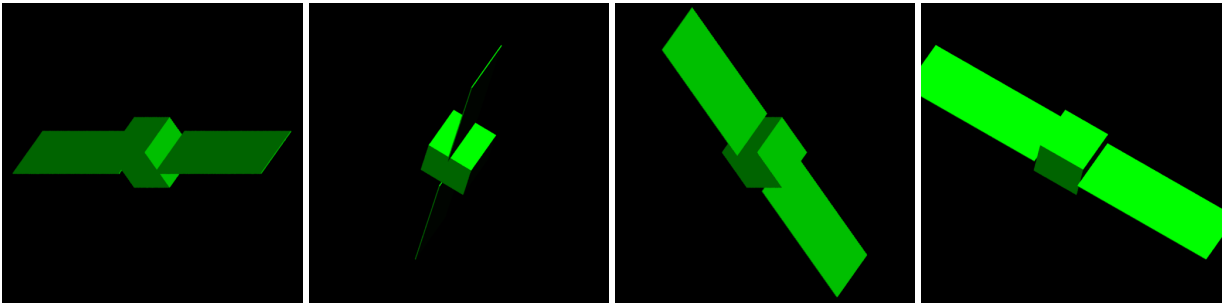


Fig. 6: Box-wing model in different orientations ( $0^\circ$ ,  $45^\circ$ ,  $90^\circ$  and  $135^\circ$ ).

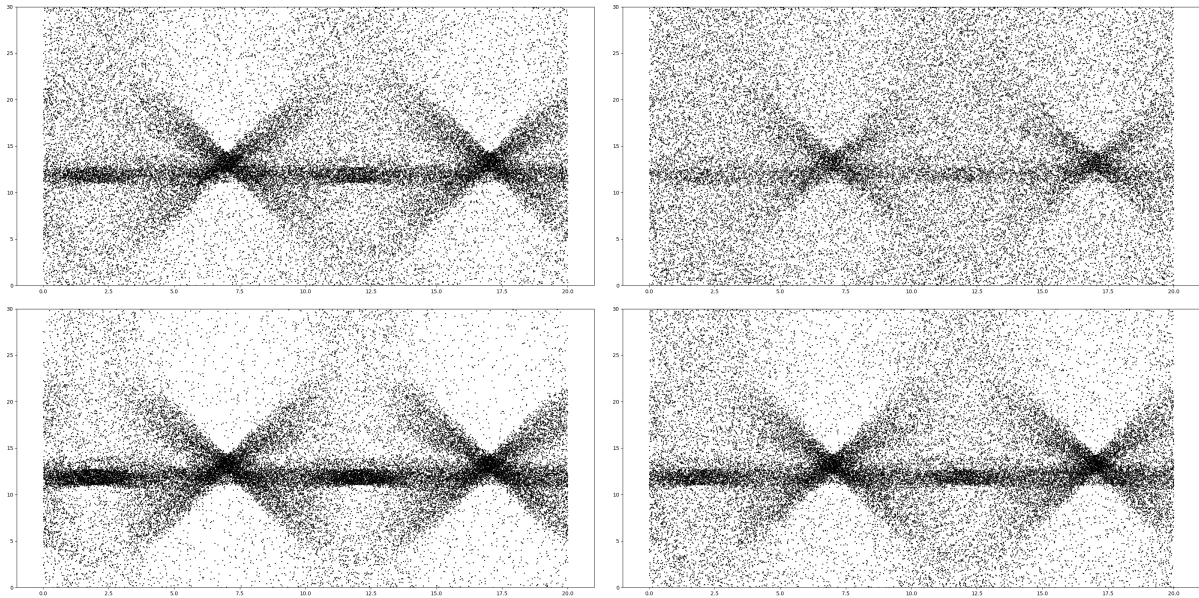


Fig. 7: As Fig. 3, for the box-wing shape model.

Our software can also model the photometry of space objects, and we are in the process of comparing its output to observed lightcurves of space debris. Comparisons with observed spectrometry are also planned. With some additional development, the polarization of light could also be taken into account in the simulation, though polarimetric observations of space objects are not commonly available. We are also developing the use of our software for radiation pressure computations, to estimate the effects of both sunlight and the outgoing radiation flux of the Earth on orbits and rotational states of space debris.

All in all, our software shows promise in modeling various interactions between light and space objects. It still requires development, but will continue to be used in future studies of debris and satellite observations at the FGI. The software will be released under a free and open source license once it reaches a stable development status.

## ACKNOWLEDGEMENTS

This work has been supported by the Academy of Finland as well as Finland's Scientific Advisory Board For Defence (MATINE).

## REFERENCES

- [1] Ludwig Combrinck. Satellite laser ranging. In Guochang Xu, editor, *Sciences of Geodesy — I Advances and Futures Directions*, chapter 9. Springer, 2010.
- [2] Scott B. Luthcke, David D. Rowlands, and Frank G. Lemoine. The SLR contribution to precise orbit determination in the GPS era. In Ron Noomen, Steven Klosko, Carey Noll, and Michael Pearlman, editors, *13th International Workshop on Laser Ranging*. NASA/CP-2003-212248, 2003.
- [3] Tim Flohrer, Beatriz Jilete, Holger Krag, Quirin Funke, Vitali Braun, and Alexandru Mancas. ESA activities on laser ranging to non-cooperative targets. In *The 2016 International Workshop on Laser Ranging, Potsdam, Germany*, October 9–14, 2016.
- [4] D. Kucharski, G. Kirchner, J. C. Bennett, M. Lachut, K. Sośnica, N. Koshkin, L. Shakun, F. Koidl, M. Steindorfer, P. Wang, C. Fan, X. Han, L. Grunwaldt, M. Wilkinson, J. Rodríguez, G. Bianco, F. Vespe, M. Catalán, K. Salmins, J. R. Pino, H.-C. Lim, E. Park, C. Moore, P. Lejba, and T. Suchodolski. Photon pressure force on space debris TOPEX/Poseidon measured by satellite laser ranging. *Earth and Space Science*, 4(10):661–668, 2017.
- [5] Matt Pharr and Greg Humphreys. *Physically Based Rendering*. Morgan Kaufman, Burlington, MA, USA, 2nd edition, 2010.
- [6] Jeff Bezanson, Alan Edelman, Stefan Karpinski, and Viral B. Shah. Julia: A fresh approach to numerical computing. *SIAM Review*, 59(1):65–98, 2017.
- [7] Michael Ashikhmin and Peter Shirley. An anisotropic Phong BRDF model. *Journal of Graphics Tools*, 5(2):23–32, 2001.
- [8] Charles J. Wetterer, Keric Hill, and Moriba Jah. Comparison of radiation pressure perturbations on rocket bodies and debris at geosynchronous earth orbit. In *Advanced Maui Optical and Space Surveillance Technologies Conference*, 2014.